

## Article

# Spectroscopic Analyses of Changes in Photocatalytic and Catalytic Activities of Mn- and Ni-Ion Doped and Base-Treated Reduced Graphene Oxide

Hangil Lee <sup>1</sup> and Hyun Sung Kim <sup>2,\*</sup><sup>1</sup> Department of Chemistry, Sookmyung Women's University, Seoul 04310, Korea; easyscan@sookmyung.ac.kr<sup>2</sup> Department of Chemistry, Pukyong National University, Busan 48513, Korea

\* Correspondence: kimhs75@pknu.ac.kr; Tel.: +82-51-629-5596

**Abstract:** While reduced graphene oxide (rGO) is used widely as a catalyst, its catalytic activity can be improved significantly by modifying it with a metal. In this study, we compared the photocatalytic and catalytic properties of base-treated rGO particles and transition-metal-ion-doped rGO based on the oxidation reaction of thiophenol and the photocatalytic degradation of 4-chlorophenol. Since the two catalytic activities are related to the changes in the electronic structure of rGO, X-ray photoemission spectroscopy, X-ray absorption spectroscopy, and Raman spectroscopy were performed. When rGO was doped with Mn<sup>2+</sup> ions, its catalytic properties improved with respect to both reactions. The changes in the electronic structure of rGO are attributed to the formation of defect structures on the rGO surface via a reaction between the doped Mn<sup>2+</sup> ions and oxygen of the rGO surface. Thus, the results show that the doping of rGO with Mn ions in the +2-charge state (stable oxide form: MnO) enhances its catalytic and photocatalytic activities. Hence, this study provides new insights into the use of defect-controlled rGO as a novel catalyst.

**Keywords:** reduced graphene oxide; photocatalyst; doping; base treatment



**Citation:** Lee, H.; Kim, H.S. Spectroscopic Analyses of Changes in Photocatalytic and Catalytic Activities of Mn- and Ni-Ion Doped and Base-Treated Reduced Graphene Oxide. *Catalysts* **2021**, *11*, 990. <https://doi.org/10.3390/catal11080990>

Academic Editors: Marcin Janczarek, Dionysios (Dion) Demetriou Dionysiou, Sami Rtimi, Ewa Kowalska and Changseok Han

Received: 28 July 2021

Accepted: 17 August 2021

Published: 18 August 2021

**Publisher's Note:** MDPI stays neutral with regard to jurisdictional claims in published maps and institutional affiliations.



**Copyright:** © 2021 by the authors. Licensee MDPI, Basel, Switzerland. This article is an open access article distributed under the terms and conditions of the Creative Commons Attribution (CC BY) license (<https://creativecommons.org/licenses/by/4.0/>).

## 1. Introduction

Reduced graphene oxide (rGO) is used extensively as a support for metal-based catalysts as well as a standalone catalyst because its surface can be readily modified with various functional groups. This is because rGO typically contains various oxygen-containing functional groups, and the electronic structure of graphene can be modified under selective conditions to make it suitable for use as an oxidative catalyst [1–13]. In addition, the activity of rGO lies between those of graphene and GO. Thus, the modification of rGO can lead to significant changes in its catalytic properties such that it can be used to control oxidation and reduction processes [14–17].

Since the catalytic properties of rGO can be improved by doping it with a metal, in this study, we pursued a strategy of doping rGO with transition metal (TM) ions to improve its catalytic properties. We doped ions of two TMs into base-treated rGO and then systematically compared the photocatalytic/catalytic activities of the doped rGO samples (TM@rGO; TM = Mn or Ni ions). We also elucidated the changes in the surface defects of rGO after doping. New catalysts based on rGO supports are being used widely in redox reactions [18–22]. In particular, rGO is being employed for photocatalytic degradation (PCD) in advanced reaction processes such as those involved in fuel cells and photosensors because of its low cost [23–27].

Controlling the defect structures of catalysts is a widely accepted strategy for enhancing their catalytic activity. The defect structure engineering of photocatalysts allows for control over their activity and thus the rate of redox reactions. In addition, defects act as mobile electron donors and can promote the activity of catalysts and photocatalysts. The role of defect structures in catalytic processes has been investigated extensively. However,

efforts are being made to further improve the catalytic activity of rGO. In particular, it has been reported that rGO doped with TM ions shows improved catalytic activity because the dopant ions increase the number of defect structures present on rGO [28–32].

The catalytic and photocatalytic activities of the TM@rGO samples fabricated in this study indicated that their properties were significantly different from those of rGO. To elucidate the reason for the observed improvements in the properties of the TM@rGO samples, their electronic structures were characterized using X-ray photoemission spectroscopy (XPS), X-ray absorption spectroscopy (XAS), and Raman spectroscopy. We also evaluated the catalytic activities of the TM@rGO samples based on the oxidation of thiophenol (TP). Finally, we analyzed their PCD activities by using them to degrade 4-chlorophenol (4-CP) under ultraviolet (UV) light. The results of the spectroscopic analyses showed that the doping of rGO with Mn ions creates defects in the rGO structure, which react well with the oxygen-containing functional groups of rGO. This increases the catalytic and photocatalytic activity of rGO.

## 2. Results

Figure 1 shows SEM images of the morphologies of rGO and the two TM@rGO composites. The rGO sample shown in Figure 1a consists of bundles, in keeping with previous reports [33–35]. The SEM images of the two TM@rGO sheets, in Figure 1b,c, show structural features that are different from those of rGO. In the case of Mn@rGO (Figure 1b), it can be seen that crystallized MnO with a cubic structure is formed on the rGO surface. In the case of Ni@rGO (Figure 1c), however, amorphous NiO is formed on the rGO surface, and the rGO flakes are deformed. The XRD patterns of the Mn@rGO and Ni@rGO is compared with that of the rGO. (Figure S1). The representative peak at  $25.5^\circ$  in all three sample appears corresponding to rGO(002). Mn@rGO exhibits a small peak at  $35.0^\circ$  corresponding to MnO (111), indicating the presence of crystalline phase of MnO but Ni@rGO did not show any additional crystalline XRD peaks. Furthermore, one can see clearly that the surface morphologies of the TM-ion-doped rGO samples are different from that of undoped rGO. Despite the changes in surface morphology after doping, surface areas of rGO, 5 wt% Mn@rGO, and 5 wt% Ni@rGO, revealed by BET analysis, were almost identical (i.e.,  $469\text{ m}^2/\text{g}$ ,  $456\text{ m}^2/\text{g}$ , and  $459\text{ m}^2/\text{g}$ , respectively (Figure S2)).

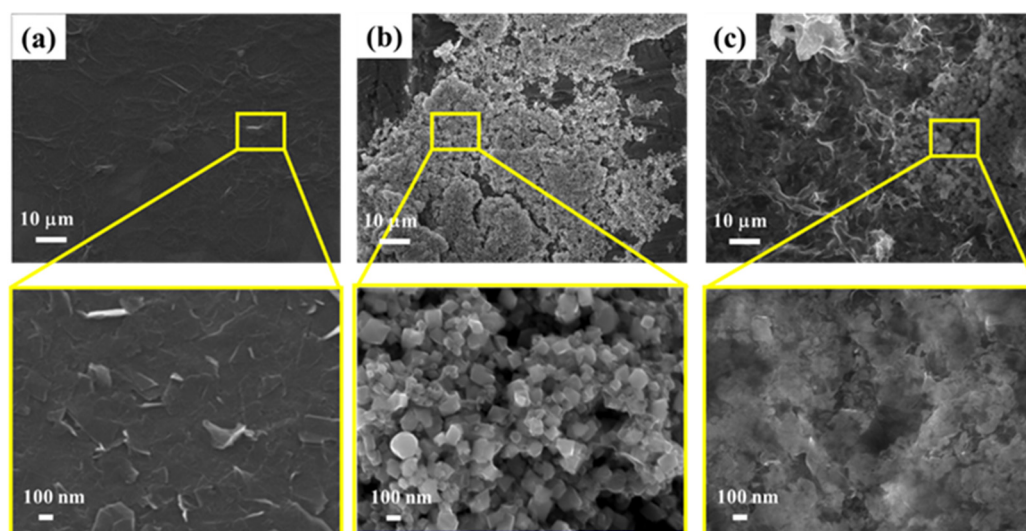


**Figure 1.** SEM images of (a) rGO, (b) 5 wt% Mn@rGO, and (c) 5 wt% Ni@rGO. Yellow boxes indicate areas corresponding to magnified images below.

We believe that the changes in the surface morphologies of the TM-ion-doped rGO samples are closely correlated to the changes in their catalytic properties. The dopants induced morphological changes on the surface of rGO, resulting in an increase in the number of active sites. This, in turn, enhanced the catalytic activity of TM@rGO. Based on the structural changes shown in Figure 1, PCD experiments were performed to investigate the activities of the modified rGO samples.

We measured the catalytic performances of the two TM@rGO samples in order to confirm their oxidative activities with respect to TP. The S 2*p* core-level spectra of Mn@rGO and Ni@rGO samples containing the respective doped metal ions in different concentrations were obtained using XPS after exposure to 180 L of TP in the presence of oxygen (see Figure 2a,b). As can be seen from the figures, these spectra contain two distinct S 2*p*<sub>3/2</sub> peaks, at 161.5 and 162.9 eV; S1 is the C–SH-related peak while S2 is the disulfide-induced peak. It is known that disulfides are the oxidation products of the thiol group [36–38]. Hence, we could monitor the catalytic activities of the TM@rGO samples by measuring the area ratios of the S1 and S2 peaks after the oxidation of TP. Figure 2a confirms that Mn@rGO is an effective oxidation catalyst. The S2/S1 area ratios for 1%, 5%, and 10 wt% Mn@rGO were 0.324, 0.413, and 0.549, respectively. The S2/S1 area ratios for 1%, 5%, and 10 wt% Ni@rGO were 0.324, 0.413, and 0.549, respectively. On the other hand, Ni@rGO did not show significant catalytic activity even when the concentration of Ni ions was increased. The fact the S2/S1 ratios for Mn@rGO were higher than those for Ni@rGO and rGO indicates that the adsorbed TP molecules were oxidized more readily on Mn@rGO. Thus, Mn@rGO is a better oxidation catalyst than rGO and Ni@rGO. Table 1 lists the S2/S1 ratios for the three rGO samples as determined during the oxidation of TP.

As mentioned above, in order to improve the photocatalytic properties of rGO, the number of defect structures present on its surface must be increased. Doping is the most effective method of achieving this because of the charge transfer between the metal-ion-doped rGO and rGO. To elucidate the changes in the number of defect structures on rGO after the doping process, we compared the PCD rates of 4-CP in Mn@rGO and Ni@rGO [39–41].

As shown in Figure 3, 4-CP degrades in the presence of both Mn@rGO and Ni@rGO. However, the PCD activity of Mn@rGO is superior to those of rGO and Ni@rGO, owing to the presence of a greater number of defect structures in this catalyst because of the doping of active Mn ions. To confirm this hypothesis, the decomposition rates of 4-CP after exposure to the different catalysts for 2 h were compared. The PCD efficiencies of the three tested samples, namely, rGO, 10 wt% Mn@rGO, and 10 wt% Ni@rGO, with respect to 4-CP were 0.844, 0.594, and 0.705, respectively. Table 2 lists these data. Thus, it was confirmed that the PCD efficiency of Mn@rGO is superior to those of rGO and Ni@rGO.

Interestingly, the catalytic activities and PCD efficiencies of the TM@rGO samples were found to be similar to the changes in the intensities of their spectral peaks during the HRPES, XAS, and Raman spectroscopy analyses. Based on these results, it should be possible to predict the catalytic activity and PCD efficiency of rGO-based catalysts from an analysis of their spectral peaks during HRPES, XAS, and Raman spectroscopy.

First, we performed XPS to compare the electronic structures of the three tested samples and to evaluate the differences in their oxygen-containing functional groups, as shown in Figure 4a. The core-level O 1s spectrum of the rGO sample indicates the presence of two typical oxygen-containing functional groups in the sample: the hydroxyl and carbonyl groups. Based on the relative electronegativity of these two groups, the peak at 533.1 eV (marked as B) was assigned to the –OH (hydroxyl) group while that at 532.0 eV (marked as A) was assigned to the –C=O (carbonyl) group [42–44]. We also found that the O 1s core level spectra of the TM@rGO samples contained peaks related to the doped TM ions at 529.9 (marked as C) and 529.5 eV (marked as D). These indicated the presence of the stable forms of the oxides (MnO and NiO) [45,46]. A comparison of the differences in the intensities of the peaks related to the two oxygen-containing functional group peaks (–OH and –C=O) yielded interesting results. We measured the B/A intensity ratios of the three

samples and found that rGO, Mn@rGO, and Ni@rGO exhibited ratios of 0.547, 0.363, and 0.445, respectively. It can be seen that the height of the peak for the –OH functional group of rGO is lower than that of the peak for the –C=O group after the doping of the TM ions. We believe the –OH groups present on the rGO surface combined with the doped TM ions to form the corresponding metal oxide (MnO or NiO). Another interesting result is that the total number of oxygen-containing groups in rGO decreased after the doping with TM ions (rGO: 1.30, Mn@rGO: 1.23, and Ni@rGO: 1.24). This suggests that a few oxygen-containing groups did not bind to the TM ions and were desorbed instead. This can be attributed to the formation of defect structures on the rGO surface.

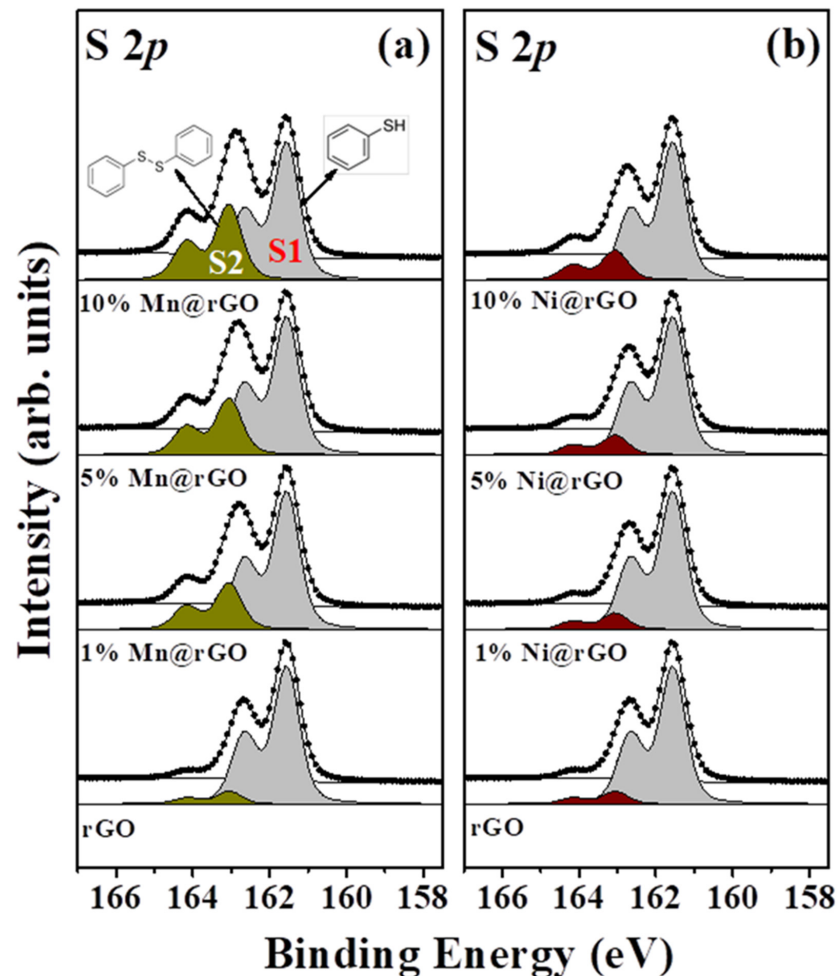


**Figure 2.** S 2p core-level spectra as determined based on catalytic oxidation of TP (360 L) in presence of (a) Mn@rGO and (b) Ni@rGO for different TM ion concentrations resulting from 360 L (1 L =  $1 \times 10^{-6}$  torr/s) exposure of TP.

**Table 1.** Catalytic activities of three rGO samples determined based on S2/S1 area ratios from S 2p core-level spectra after oxidation of TP (S2/S1).

rGO	Doping Amount	Mn@rGO	Ni@rGO
$0.095 \pm 0.01$	TM ion 1%	$0.324 \pm 0.05$	$0.119 \pm 0.05$
-	TM ion 5%	$0.413 \pm 0.05$	$0.132 \pm 0.05$
-	TM ion 10%	$0.549 \pm 0.05$	$0.229 \pm 0.05$

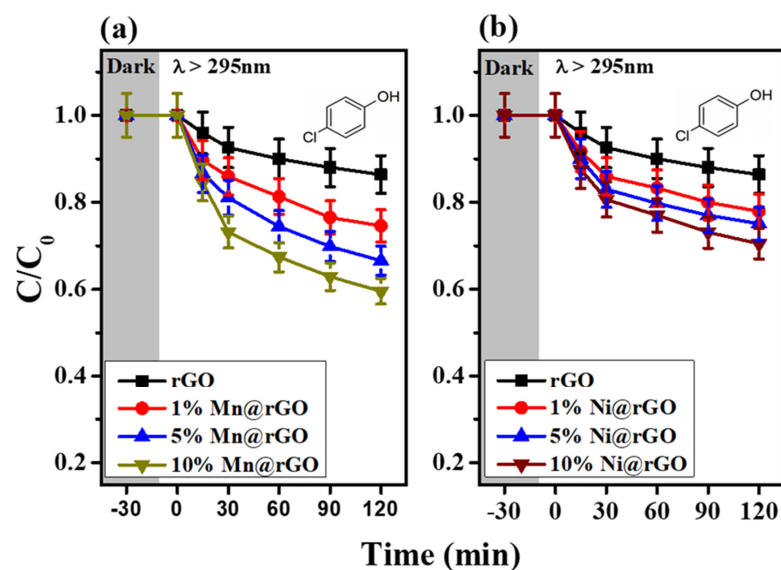


**Figure 3.** PCD of 4-CP using (a) Mn@rGO and (b) Ni@rGO with different dopant ion concentrations. [rGO] = 0.5 g/L,  $\lambda \geq 295$  nm, [4-CP]<sub>0</sub> = 10  $\mu$ M.

**Table 2.** PCD efficiencies, 4-CP ( $C/C_0$ ) of three rGO samples with to 4-CP (degradation time of 2 h).

rGO	Doping Amount	Mn@rGO	Ni@rGO
0.844 ± 0.05	TM ion 1%	0.746 ± 0.05	0.779 ± 0.05
-	TM ion 5%	0.665 ± 0.05	0.751 ± 0.05
-	TM ion 10%	0.594 ± 0.05	0.705 ± 0.05

Next, the O K-edge XAS spectra of the three samples were measured, as shown in Figure 4b. The figure shows four primary resonance peaks, at approximately 530.1 (marked as E), 531.8 (marked as F), 535.2 (marked as G), and 537.5 eV (marked as H), as well as a collection of peaks centered at approximately 543.4 eV (marked as I). The lower-energy absorption edges, namely, those seen at 530.1 (E) and 531.8 eV (F), are the  $\pi^*$  resonances of the C=O or COOH peaks of carbon [47–49]. The peak located at 535.2 eV (marked as G) and the broad peak located at 537.5 eV (marked as H) are ascribable to an O–H-related  $\sigma^*$  state, that is, a single-bonded oxygen (e.g., C–OH)  $\sigma^*$  state. The broad feature at approximately 543.4 eV (marked as I) is related to a carbonyl  $\sigma^*$  state (C=O). The most notable change in the XAS spectra is the change in the  $\sigma^*$  orbital peak, which is related to the OH groups present in rGO, after the doping of the TM ions. Compared with the intensity of the main resonance peak of rGO, that of peak I, which corresponds to the C=O orbital, is significantly lower. However, the decrease in the intensity of peak H, which corresponds to the OH orbital, is larger. More specifically, on comparing the results for Mn@rGO with those for rGO, it can be seen that the intensity of the H peak associated with the -OH group is significantly reduced in the case of the former. To analyze the unoccupied electronic structures of the TM-ion-doped rGO samples in detail, we measured their Mn and Ni L-edge XAS spectra (see inset of Figure 4b). The Mn L-edge XAS spectrum in Figure 4b contains three distinct peaks, at 639.6, 641.1.0, and 643.3 eV, which correspond to the typical  $Mn^{2+}$   $L_3$ -edge structures of MnO. In addition, the sharp Ni  $L_3$  peaks at 850.2 and 852.2 eV in Figure 4b correspond to the  $Ni^{2+}$   $L_3$ -edge structures of NiO [50–53]. These spectra indicate that the electronic states of the doped Mn and Ni ions corresponded to those in MnO and NiO, respectively.

Figure 4c shows the Raman spectra of rGO, Mn@rGO, and Ni@rGO. The G-peak (1580  $cm^{-1}$ ) and D-peak (1320  $cm^{-1}$ ) in the Raman spectrum of rGO can be attributed to the  $E_{2g}$  phonons at the Brillouin zone centers and the breathing mode of  $sp^2$ -carbon atoms, respectively [54–56]. The differences in the electronic structures of the three samples can be

seen in Figure 4. The following three features of the spectra are apparent in Figure 4c: the changes in the intensity ratio of the D and G peaks and the changes in the intensities of the 2D and D + G peaks. To begin with, based on the intensity ratio of the D and G peaks, it can be seen that the ratios for the TM@rGO samples are lower than that for rGO (the D/G intensity ratios of rGO, Mn@rGO, and Ni@rGO are 1.761, 1.10, and 1.567, respectively). This indicates a decrease in the concentrations of the oxygen-containing functional groups on the surface of rGO. More specifically, rGO is converted into a graphene-like form because the doped TM ions react with these oxygen-containing functional groups, resulting in a decrease in the amount of available oxygen. This can be explained by the fact that the catalytic properties of rGO itself change through a reaction with the doped TM ions. Secondly, the electronic structure of the doped TM ions and their concentration vary. As can be seen from the figure, the Mn- and Ni-doped samples exhibit peaks at 659 and 531  $\text{cm}^{-1}$ , respectively; these are related to MnO and NiO, respectively. [57–60] Interestingly, even though the two TMs were doped in the same concentration, the amounts converted into their respective metal oxides differed. In other words, the amount of MnO formed was approximately 2.5 times greater than that of NiO. This result seems to be directly related to the changes in the catalytic and photocatalytic properties of rGO. Thirdly, there are changes in the 2D and D + G peaks, which provide information about the multilayer rGO, and almost disappear when doped with Mn ions. This result indicates that the activity of the doped Mn ions is higher than that of the doped Ni ions. Thus, the doped Mn ions reacted with the oxygen-containing functional groups on the surface of rGO, thus affecting its catalytic activity.

Hence, the observed changes in the catalytic properties can be explained by the changes in the availability of OH groups because of the reactions of the doped ions with these groups during the doping process. In particular, doping with Mn resulted in greater changes than doping with Ni because the reaction between the Mn ions and rGO was a stronger one than that between the Ni ions and rGO. Therefore, the differences in the catalytic and photocatalytic activities of the three samples can be explained based on the differences in the results of their spectroscopic analyses. In conclusion, based on the measurement results of two different parameters, namely, the catalytic oxidation rate of TP and the PCD rate of 4-CP, we could confirm that the activity of Mn-doped rGO in both cases is higher than those of rGO and Ni-doped rGO.

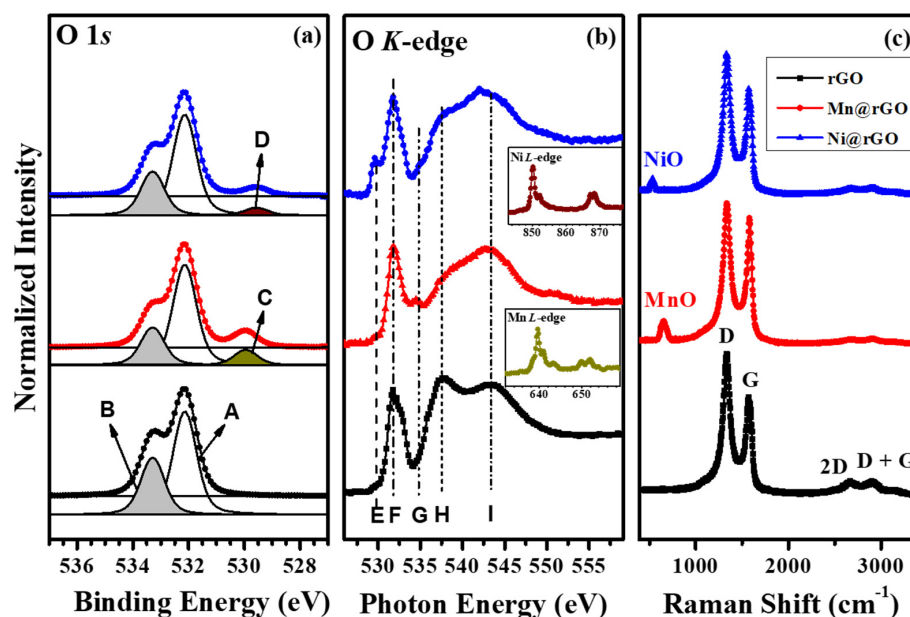


Figure 4. (a) HRPES, (b) XAS, and (c) Raman spectra of rGO (black), 5 wt% Mn@rGO (red), and 5 wt% Ni@rGO (blue); insets of (b) show Mn and Ni L-edge XAS spectra.

### 3. Materials and Methods

#### 3.1. Preparation of TM@rGO Solutions

First, rGO was obtained from GO using Hummers' method, which involved adding hydrazine (1.0 mL) to a dispersion of GO (50 mg of GO in 100 mL of water) [61,62]. After obtaining rGO, we subjected it to a base treatment (pH = 13.0) to increase the number of defects and form more -OH functional groups on its surface. Next, rGO was sintered for 30 min at 90 °C, and the dopant TM ions (Mn or Ni) were added to a solution of rGO at 90 °C. The solution was stirred until it became transparent (1 h). The thus-obtained gel solution was transferred to an autoclave and heated at 220 °C for 7 h in a convection oven. The resulting TM@rGO sample (Mn@rGO or Ni@rGO) was filtered and washed with double-distilled water to remove any residue present.

#### 3.2. Preparation of TM-Ion-Doped rGO

For the doping process, the desired amounts of the TM ions (wt% with respect to rGO (i.e.,  $TM/(TM + rGO)$ )) were added to a solution of rGO in the form  $TM(NO_3)_x \cdot nH_2O$  (metal nitrate n-hydrate).  $Mn(NO_3)_2 \cdot xH_2O$  (98%),  $Ni(NO_3)_2 \cdot 6H_2O$  ( $\geq 98\%$ ), TP (99% purity), and 4-CP ( $\geq 99\%$ ) were purchased from Sigma-Aldrich (Burlington, MA, USA).

#### 3.3. Photocatalytic Measurements

We used 4-CP as the target contaminant. Suspensions of the contaminant were stirred magnetically in the dark for 30 min to establish an equilibrium between the absorption and desorption processes. The three different rGO samples were dispersed in distilled water ( $0.5 \text{ g L}^{-1}$ ) under sonication. A 300W Xe arc lamp (Oriel, Andover, MA, USA) was employed as the light source, which was used in combination with a 10-cm infrared water filter and a cut-off filter ( $\lambda > 295 \text{ nm}$  for UV light). The changes in the concentration of 4-CP were measured by high-performance liquid chromatography (UFLC LC-20AD pump, Shimadzu, Kyoto, Japan).

#### 3.4. Characterization

Scanning electron microscopy (SEM) images of the samples were obtained using a field-emission SEM system (JSM-7600F, JEOL, Tokyo, Japan) operated at an acceleration voltage of 15 kV. High-resolution photoemission spectroscopy (HRPES) measurements were performed at beamline 10A2 of the Pohang Accelerator Laboratory (PAL). The S 2p and O 1s core level spectra were obtained at photon energies of 230 and 580 eV, respectively. XAS was also performed at beamline 10A2 to obtain the O K-edge spectra. The Raman spectral data were obtained using an  $Ar^+$  ion laser (Stabilite 2017;  $\lambda_{ex} = 514.5 \text{ nm}$ , Spectra-Physics, Andover, MA, USA) excitation source connected to a TRIAX 550 spectrometer (Horiba Jobin Yvon, Kyoto, Japan).

### 4. Conclusions

We compared the catalytic activities of pristine rGO and rGO samples doped with two TMs based on the oxidation of TP and the PCD of 4-CP in their presence. Using various spectroscopic analysis techniques, it was confirmed that the PCD and oxidative activities of Mn@rGO are higher than those of pristine rGO and Ni@rGO. These results indicate that the number density of the defect structures of Mn@rGO is greater than those of pristine rGO and Ni@rGO. This, in turn, can be attributed to the higher reactivity between rGO and the doped Mn ions, which improves the catalytic and photocatalytic properties of rGO. Thus, the use of spectroscopic methods for the precise analysis of the defect structures of rGO-based catalysts is recommended for the development of high-performance catalysts.

**Supplementary Materials:** The following are available online at <https://www.mdpi.com/article/10.3390/catal11080990/s1>, Figure S1: XRD Data, Figure S2: N<sub>2</sub> adsorption and desorption isotherm plots.

**Author Contributions:** H.L. performed the experiments; H.L. and H.S.K. analyzed the data; and wrote the paper. Both authors have read and agreed to the published version of the manuscript.

**Funding:** This work was supported by the National Research Foundation of Korea (NRF) grant funded by the Korean government (MSIT) (2021R1A2C2007992, and NRF-2020R1A2C1010725). This work was also supported by MSIT and PAL.

**Conflicts of Interest:** The authors declare no conflict of interest.

## References

1. Zhou, M.; Han, D.; Liu, X.; Ma, C.; Wang, H.; Tang, Y.; Huo, P.; Shi, W.; Yan, Y.; Yang, J. Enhanced visible light photocatalytic activity of alkaline earth metal ions-doped CdSe/rGO photocatalysts synthesized by hydrothermal method. *Appl. Catal. B Environ.* **2015**, *172–173*, 174–184. [[CrossRef](#)]
2. Becerril, H.A.; Mao, J.; Liu, Z.; Stoltenberg, R.M.; Bao, Z.; Chen, Y. Evaluation of solution-processed reduced graphene oxide films as transparent conductors. *ACS Nano* **2008**, *2*, 463–470. [[CrossRef](#)] [[PubMed](#)]
3. He, D.; Jiang, Y.; Lv, H.; Pan, M.; Mu, S. Nitrogen-doped reduced graphene oxide supports for noble metal catalysts with greatly enhanced activity and stability. *Appl. Catal. B Environ.* **2013**, *132–133*, 379–388. [[CrossRef](#)]
4. Song, Z.; Sun, J.; Wang, W.; Wang, Z.; Zhang, Y.; Xu, B.; Qi, F. Stable synergistic decontamination and self-cleaning performance of powerful N-rGO catalytic ozonation membrane: Clustering effect of free electrons and role of interface properties. *Appl. Catal. B Environ.* **2021**, *283*, 119662. [[CrossRef](#)]
5. Men, S.; Zheng, H.; Ma, D.; Huang, X.; Kang, X. Unraveling the stabilization mechanism of solid electrolyte interface on ZnSe by rGO in sodium ion battery. *J. Energy Chem.* **2021**, *54*, 124–130. [[CrossRef](#)]
6. Chandra, V.; Park, J.; Chun, Y.; Lee, J.W.; Hwang, I.; Kim, K.S. Water-Dispersible Magnetite-Reduced Graphene Oxide Composites for Arsenic Removal. *ACS Nano* **2010**, *4*, 3979–3986. [[CrossRef](#)]
7. Liu, X.; Dai, L. Carbon-based metal-free catalysts. *Nat. Rev. Mater.* **2016**, *1*, 16064. [[CrossRef](#)]
8. Pei, Y.; Song, H.; Liu, Y.; Cheng, Y.; Li, W.; Chen, Y.; Fan, Y.; Liu, B.; Lu, S. Boron–nitrogen-doped carbon dots on multi-walled carbon nanotubes for efficient electrocatalysis of oxygen reduction reactions. *J. Colloid Interface Sci.* **2021**, *600*, 865–871. [[CrossRef](#)]
9. Lin, Y.C.; Peng, C.K.; Lim, S.C.; Chen, C.L.; Nguyễn, T.N.; Wang, T.T.; Lin, M.C.; Hsu, Y.J.; Chen, S.Y.; Lin, Y.G. Tailoring the surface oxygen engineering of a carbon-quantum-dot-sensitized ZnO@H-ZnO<sub>1-x</sub> multijunction toward efficient charge dynamics and photoactivity enhancement. *Appl. Catal. B Environ.* **2021**, *285*, 119846. [[CrossRef](#)]
10. Xue, Y.; Huang, B.; Yi, Y.; Guo, Y.; Zuo, Z.; Li, Y.; Jia, Z.; Liu, H.; Li, Y. Anchoring zero valence single atoms of nickel and iron on graphdiyne for hydrogen evolution. *Nat. Commun.* **2018**, *9*, 1460. [[CrossRef](#)]
11. Hui, L.; Xue, Y.; Yu, H.; Liu, Y.; Fang, Y.; Xing, C.; Huang, B.; Li, Y. Highly Efficient and Selective Generation of Ammonia and Hydrogen on a Graphdiyne-Based Catalyst. *J. Am. Chem. Soc.* **2019**, *141*, 10677–10683. [[CrossRef](#)]
12. Paul, R.; Zhu, L.; Chen, H.; Qu, J.; Dai, L. Recent Advances in Carbon-Based Metal-Free Electrocatalysts. *Adv. Mater.* **2019**, *31*, 1806403. [[CrossRef](#)]
13. Hu, C.; Dai, L. Doping of Carbon Materials for Metal-Free Electrocatalysis. *Adv. Mater.* **2019**, *31*, 1804672. [[CrossRef](#)] [[PubMed](#)]
14. Moon, I.K.; Lee, J.; Ruoff, R.S.; Lee, H. Reduced graphene oxide by chemical graphitization. *Nat. Commun.* **2010**, *1*, 73. [[CrossRef](#)]
15. Pei, S.; Cheng, H.M. The reduction of graphene oxide. *Carbon* **2012**, *50*, 3210–3228. [[CrossRef](#)]
16. Lightcap, I.V.; Kosel, T.H.; Kamat, P.V. Anchoring semiconductor and metal nanoparticles on a two-dimensional catalyst mat. storing and shuttling electrons with reduced graphene oxide. *Nano Lett.* **2010**, *10*, 577–583. [[CrossRef](#)] [[PubMed](#)]
17. Meng, F.; Li, J.; Cushing, S.K.; Zhi, M.; Wu, N. Solar hydrogen generation by nanoscale p-n junction of p-type molybdenum disulfide/n-type nitrogen-doped reduced graphene oxide. *J. Am. Chem. Soc.* **2013**, *135*, 10286–10289. [[CrossRef](#)]
18. Dubey, S.P.; Nguyen, T.T.M.; Kwon, Y.N.; Lee, C. Synthesis and characterization of metal-doped reduced graphene oxide composites, and their application in removal of Escherichia coli, arsenic and 4-nitrophenol. *J. Ind. Eng. Chem.* **2015**, *29*, 282–288. [[CrossRef](#)]
19. Banerjee, P.C.; Lobo, D.E.; Middag, R.; Ng, W.K.; Shaibani, M.E.; Majumder, M. Electrochemical capacitance of Ni-doped metal organic framework and reduced graphene oxide composites: More than the sum of its parts. *ACS Appl. Mater. Interfaces* **2015**, *7*, 3655–3664. [[CrossRef](#)]
20. Said, Z.; Ghodbane, M.; Sundar, L.S.; Tiwari, A.K.; Sheikholeslami, M.; Boumeddane, B. Heat transfer, entropy generation, economic and environmental analyses of linear fresnel reflector using novel rGO-Co<sub>3</sub>O<sub>4</sub> hybrid nanofluids. *Renew. Energy* **2021**, *165*, 420–437. [[CrossRef](#)]
21. Park, S.W.; Shin, H.J.; Heo, Y.J.; Kim, D.W. Rational design of S, N Co-doped reduced graphene oxides/pyrrhotite Fe<sub>7</sub>S<sub>8</sub> as free-standing anodes for large-scale, ultrahigh-rate and long-lifespan Li- and Na-ion batteries. *Appl. Surf. Sci.* **2021**, *540*, 148358. [[CrossRef](#)]
22. Zhang, G.; Xia, B.Y.; Wang, X.; Lou, X.W. Strongly coupled NiCo<sub>2</sub>O<sub>4</sub>-rGO hybrid nanosheets as a methanol-tolerant electrocatalyst for the oxygen reduction reaction. *Adv. Mater.* **2014**, *26*, 2408–2412. [[CrossRef](#)]

23. Fan, W.; Yu, X.; Lu, H.C.; Bai, H.; Zhang, C.; Shi, W. Fabrication of TiO<sub>2</sub>/RGO/Cu<sub>2</sub>O heterostructure for photoelectrochemical hydrogen production. *Appl. Catal. B Environ.* **2016**, *181*, 7–15. [[CrossRef](#)]
24. Dixit, T.K.; Sharma, S.; Sinha, A.S.K. Synergistic effect of N-rGO supported Gd doped bismuth ferrite heterojunction on enhanced photocatalytic degradation of rhodamine B. *Mater. Sci. Semicond. Process.* **2021**, *123*, 105538. [[CrossRef](#)]
25. Fresno, F.; Iglesias, O.; Alfonso-González, E.; Rivero, M.J.; Ortiz, I.; de la Peña O'Shea, V.A. Assessing the feasibility of reduced graphene oxide as an electronic promoter for photocatalytic hydrogen production over Nb-Ta perovskite photocatalysts. *Catal. Today* **2021**, *362*, 22–27. [[CrossRef](#)]
26. Li, Y.; Zhang, H.; Liu, P.; Wang, D.; Li, Y.; Zhao, H. Cross-linked g-C<sub>3</sub>N<sub>4</sub>/rGO nanocomposites with tunable band structure and enhanced visible light photocatalytic activity. *Small* **2013**, *9*, 3336–3344. [[CrossRef](#)]
27. Yu, J.; Jin, J.; Cheng, B.; Jaroniec, M. A noble metal-free reduced graphene oxide-CdS nanorod composite for the enhanced visible-light photocatalytic reduction of CO<sub>2</sub> to solar fuel. *J. Mater. Chem. A* **2014**, *2*, 3407–3416. [[CrossRef](#)]
28. Zou, W.; Zhang, L.; Liu, L.; Wang, X.; Sun, J.; Wu, S.; Deng, Y.; Tang, C.; Gao, F.; Dong, L. Engineering the Cu<sub>2</sub>O-reduced graphene oxide interface to enhance photocatalytic degradation of organic pollutants under visible light. *Appl. Catal. B Environ.* **2016**, *181*, 495–503. [[CrossRef](#)]
29. Zhu, J.; Ren, Z.; Du, S.; Xie, Y.; Wu, J.; Meng, H.; Xue, Y.; Fu, H. Co-vacancy-rich Co<sub>1-x</sub>S nanosheets anchored on rGO for high-efficiency oxygen evolution. *Nano Res.* **2017**, *10*, 1819–1831. [[CrossRef](#)]
30. Kim, H.W.; Park, H.; Roh, J.S.; Shin, J.E.; Lee, T.H.; Zhang, L.; Cho, Y.H.; Yoon, H.W.; Bukas, V.J.; Guo, J.; et al. Carbon Defect Characterization of Nitrogen-Doped Reduced Graphene Oxide Electrocatalysts for the Two-Electron Oxygen Reduction Reaction. *Chem. Mater.* **2019**, *31*, 3967–3973. [[CrossRef](#)]
31. Shah, S.A.; Zhu, G.; Shen, X.; Kong, L.; Ji, Z.; Xu, K.; Zhou, H.; Zhu, J.; Song, P.; Song, C.; et al. Controllable Sandwiching of Reduced Graphene Oxide in Hierarchical Defect-Rich MoS<sub>2</sub> Ultrathin Nanosheets with Expanded Interlayer Spacing for Electrocatalytic Hydrogen Evolution Reaction. *Adv. Mater. Interfaces* **2018**, *5*, 1801093. [[CrossRef](#)]
32. Kumar, E.T.D.; Easwaramoorthi, S.; Rao, J.R. Fluorinated Reduced Graphene Oxide-Encapsulated ZnO Hollow Sphere Composite as an Efficient Photocatalyst with Increased Charge-Carrier Mobility. *Langmuir* **2019**, *35*, 8681–8691. [[CrossRef](#)]
33. Wang, Z.; Zhang, F.; Zou, H.; Yuan, Y.; Wang, H.; Xia, J.; Wang, Z. Preparation of a Pt/NiFe layered double hydroxide/reduced graphene oxide composite as an electrocatalyst for methanol oxidation. *J. Electroanal. Chem.* **2018**, *818*, 198–203. [[CrossRef](#)]
34. Wei, M.; Qiao, L.; Zhang, H.; Karakalos, S.; Ma, K.; Fu, Z.; Swihart, M.T.; Wu, G. Engineering reduced graphene oxides with enhanced electrochemical properties through multiple-step reductions. *Electrochim. Acta* **2017**, *258*, 735–743. [[CrossRef](#)]
35. Gaidukevič, J.; Pauliukaitė, R.; Niaura, G.; Matulaitienė, I.; Opuchovič, O.; Radzevič, A.; Astromskas, G.; Bukauskas, V.; Barkauskas, J. Synthesis of reduced graphene oxide with adjustable microstructure using regioselective reduction in the melt of boric acid: Relationship between structural properties and electrochemical performance. *Nanomaterials* **2018**, *8*, 889. [[CrossRef](#)]
36. Qiao, R.; Chin, T.; Harris, S.J.; Yan, S.; Yang, W. Spectroscopic fingerprints of valence and spin states in manganese oxides and fluorides. *Curr. Appl. Phys.* **2013**, *13*, 544–548. [[CrossRef](#)]
37. Barriet, D.; Yam, C.M.; Shmakova, O.E.; Jamison, A.C.; Lee, T.R. 4-mercaptophenylboronic acid SAMs on gold: Comparison with SAMs derived from thiophenol, 4-mercaptophenol, and 4-mercaptobenzoic acid. *Langmuir* **2007**, *23*, 8866–8875. [[CrossRef](#)]
38. Ren, R.; Li, S.; Li, J.; Ma, J.; Liu, H.; Ma, J. Enhanced catalytic activity of Au nanoparticles self-assembled on thiophenol functionalized graphene. *Catal. Sci. Technol.* **2015**, *5*, 2149–2156. [[CrossRef](#)]
39. Çatalakaya, E.Ç.; Bali, U.; Şengül, F. Photochemical degradation and mineralization of 4-chlorophenol. *Environ. Sci. Pollut. Res.* **2003**, *10*, 113–120. [[CrossRef](#)]
40. Rajar, K.; Balouch, A.; Bhangar, M.I.; Sherazi, T.H.; Kumar, R. Degradation of 4-Chlorophenol Under Sunlight Using ZnO Nanoparticles as Catalysts. *J. Electron. Mater.* **2018**, *47*, 2177–2183. [[CrossRef](#)]
41. Ezhilarasi, A.A.; Judith Vijaya, J.; Kaviyarasu, K.; John Kennedy, L.; Ramalingam, R.J.; Al-Lohedan, H.A. Green synthesis of NiO nanoparticles using Aegle marmelos leaf extract for the evaluation of in-vitro cytotoxicity, antibacterial and photocatalytic properties. *J. Photochem. Photobiol. B Biol.* **2018**, *180*, 39–50. [[CrossRef](#)]
42. Kim, M.; Lee, C.; Jang, J. Fabrication of highly flexible, scalable, and high-performance supercapacitors using polyaniline/reduced graphene oxide film with enhanced electrical conductivity and crystallinity. *Adv. Funct. Mater.* **2014**, *24*, 2489–2499. [[CrossRef](#)]
43. Sun, Y.; Ding, C.; Cheng, W.; Wang, X. Simultaneous adsorption and reduction of U(VI) on reduced graphene oxide-supported nanoscale zerovalent iron. *J. Hazard. Mater.* **2014**, *280*, 399–408. [[CrossRef](#)]
44. Lerf, A.; He, H.; Forster, M.; Klinowski, J. Structure of graphite oxide revisited. *J. Phys. Chem. B* **1998**, *102*, 4477–4482. [[CrossRef](#)]
45. Badyal, J.P.S.; Zhang, X.; Lambert, R.M. A model oxide catalyst system for the activation of methane: Lithium-doped NiO on Ni(111). *Surf. Sci. Lett.* **1990**, *225*, 15–19. [[CrossRef](#)]
46. Uhlenbrock, S.; Scharfschwerdt, C.; Neumann, M.; Illing, G.; Freund, H.J. The influence of defects on the Ni 2p and O 1s XPS of NiO. *J. Phys. Condens. Matter* **1992**, *4*, 7973–7978. [[CrossRef](#)]
47. Ma, C.; Xu, J.; Alvarado, J.; Qu, B.; Somerville, J.; Lee, J.Y.; Meng, Y.S. Investigating the Energy Storage Mechanism of SnS<sub>2</sub>-rGO Composite Anode for Advanced Na-Ion Batteries. *Chem. Mater.* **2015**, *27*, 5633–5640. [[CrossRef](#)]
48. Pettong, T.; Iamprasertkun, P.; Krittayavathananon, A.; Sukha, P.; Sirisinudomkit, P.; Seubsai, A.; Chareonpanich, M.; Kongkachuichay, P.; Limtrakul, J.; Sawangphruk, M. High-Performance Asymmetric Supercapacitors of MnCo<sub>2</sub>O<sub>4</sub> Nanofibers and N-Doped Reduced Graphene Oxide Aerogel. *ACS Appl. Mater. Interfaces* **2016**, *8*, 34045–34053. [[CrossRef](#)]

49. Kim, Y.; Noh, Y.; Lim, E.J.; Lee, S.; Choi, S.M.; Kim, W.B. Star-shaped Pd@Pt core-shell catalysts supported on reduced graphene oxide with superior electrocatalytic performance. *J. Mater. Chem. A* **2014**, *2*, 6976–6986. [[CrossRef](#)]
50. Yabuuchi, N.; Yoshii, K.; Myung, S.T.; Nakai, I.; Komaba, S. Detailed studies of a high-capacity electrode material for rechargeable batteries,  $\text{Li}_2\text{MnO}_3\text{-LiCo}_{1/3}\text{Ni}_{1/3}\text{Mn}_{1/3}\text{O}_2$ . *J. Am. Chem. Soc.* **2011**, *133*, 4404–4419. [[CrossRef](#)]
51. Yu, X.; Lyu, Y.; Gu, L.; Wu, H.; Bak, S.-M.; Zhou, Y.; Amine, K.; Ehrlich, S.N.; Li, H.; Nam, K.-W.; et al. Understanding the Rate Capability of High-Energy-Density Li-Rich Layered  $\text{Li}_{1.2}\text{Ni}_{0.15}\text{Co}_{0.1}\text{Mn}_{0.55}\text{O}_2$  Cathode Materials. *Adv. Energy Mater.* **2014**, *4*, 1300950. [[CrossRef](#)]
52. Regan, T.J.; Ohldag, H.; Stamm, C.; Nolting, F.; Lüning, J.; Stöhr, J.; White, R.L. Chemical effects at metal/oxide interfaces studied by x-ray-absorption spectroscopy. *Phys. Rev. B* **2001**, *64*, 214422. [[CrossRef](#)]
53. Nam, K.W.; Yoon, W.S.; Kim, K.B. X-ray absorption spectroscopy studies of nickel oxide thin film electrodes for supercapacitors. *Electrochim. Acta* **2002**, *47*, 3201–3209. [[CrossRef](#)]
54. Ramesha, G.K.; Sampath, N.S. Electrochemical reduction of oriented Graphene oxide films: An in situ Raman Spectro electrochemical study. *J. Phys. Chem. C* **2009**, *113*, 7985–7989. [[CrossRef](#)]
55. Shen, J.; Yan, B.; Shi, M.; Ma, H.; Li, N.; Ye, M. One step hydrothermal synthesis of  $\text{TiO}_2$ -reduced graphene oxide sheets. *J. Mater. Chem.* **2011**, *21*, 3415–3421. [[CrossRef](#)]
56. Singh, V.K.; Shukla, A.; Patra, M.K.; Saini, L.; Jani, R.K.; Vadera, S.R.; Kumar, N. Microwave absorbing properties of a thermally reduced graphene oxide/nitrile butadiene rubber composite. *Carbon* **2012**, *50*, 2202–2208. [[CrossRef](#)]
57. Zhang, K.; Han, P.; Gu, L.; Zhang, L.; Liu, Z.; Kong, Q.; Zhang, C.; Dong, S.; Zhang, Z.; Yao, J.; et al. Synthesis of nitrogen-doped  $\text{MnO}$ /graphene nanosheets hybrid material for lithium ion batteries. *ACS Appl. Mater. Interfaces* **2012**, *4*, 658–664. [[CrossRef](#)]
58. Ramesh, K.; Chen, L.; Chen, F.; Liu, Y.; Wang, Z.; Han, Y.F. Re-investigating the CO oxidation mechanism over unsupported  $\text{MnO}$ ,  $\text{Mn}_2\text{O}_3$  and  $\text{MnO}_2$  catalysts. *Catal. Today* **2008**, *131*, 477–482. [[CrossRef](#)]
59. Zhou, G.; Wang, D.W.; Yin, L.C.; Li, N.; Li, F.; Cheng, H.M. Oxygen bridges between  $\text{NiO}$  nanosheets and graphene for improvement of lithium storage. *ACS Nano* **2012**, *6*, 3214–3223. [[CrossRef](#)]
60. Zhang, Z.; Shao, C.; Li, X.; Wang, C.; Zhang, M.; Liu, Y. Electrospun nanofibers of p-type  $\text{NiO}$ /n-type  $\text{ZnO}$  heterojunctions with enhanced photocatalytic activity. *ACS Appl. Mater. Interfaces* **2010**, *2*, 2915–2923. [[CrossRef](#)]
61. Zhao, Y.; Zhang, X.; Wang, T.; Song, T.; Yang, P. Fabrication of  $\text{rGO}/\text{CdS}@2\text{H}, 1\text{T}$ , amorphous  $\text{MoS}_2$  heterostructure for enhanced photocatalytic and electrocatalytic activity. *Int. J. Hydrogen Energy* **2020**, *45*, 21409–21421. [[CrossRef](#)]
62. Hummers, W.S.; Offeman, R.E. Preparation of Graphitic Oxide. *J. Am. Chem. Soc.* **1958**, *80*, 1339. [[CrossRef](#)]